

# Supporting Information

## Back-reflected performance-enhanced flexible perovskite photodetectors through substrate texturing with femtosecond laser

*Ye Wang<sup>1,2</sup>, Wenwei Liu<sup>3</sup>, Wei Xin<sup>1\*</sup>, Tingting Zou<sup>1,2</sup>, Xin Zheng<sup>1,2</sup>, Yanshuang Li<sup>2,4</sup>, Xiuhua Xie<sup>4</sup>, Xiaojuan Sun<sup>4</sup>, Weili Yu<sup>1</sup>, Zhibo Liu<sup>3</sup>, Shuqi Chen<sup>3\*</sup>, Jianjun Yang<sup>1\*</sup>, Chunlei Guo<sup>1,5\*</sup>*

1. State Key Laboratory for Applied Optics, Changchun Institute of Optics, Fine Mechanics and Physics, Chinese Academy of Sciences, Changchun, China, 130033
2. Center of Materials Science and Optoelectronics Engineering, University of Chinese Academy of Sciences, Beijing, China, 100049
3. The Key Laboratory of Weak Light Nonlinear Photonics Ministry of Education, Teda Applied Physics Institute and School of Physics, Nankai University, Tianjin, China, 300071
4. State Key Laboratory of Luminescence and Applications, Changchun Institute of Optics, Fine Mechanics and Physics, Chinese Academy of Sciences, Changchun, China, 130033
5. The Institute of Optics, University of Rochester, Rochester, NY 14627, USA

ORCID:

Wei Xin: 0000-0002-1887-7535

Weili Yu: 0000-0001-5075-9638

Zhi-Bo Liu: 0000-0001-9210-156X

Shuqi Chen: 0000-0002-7898-4148

Jianjun Yang: 0000-0002-6703-4403

Chun-lei Guo: 0000-0001-8525-6301

\*To whom correspondence should be addressed.

E-mail: weixin@ciomp.ac.cn; schen@nankai.edu.cn; jjyang@ciomp.ac.cn;

guo@optics.rochester.edu



## **Supporting Information S1**

### **Universal near-field electric field enhancement of the structured PET**

In order to further understand the optical enhancement characteristics of the structured PET grating structures, we simulated the near-field electric field distribution of PET gratings with different widths and depths, as shown in Figure S1. The optical parameters of the PET, such as the refractive index ( $n$ ) and extinction coefficient ( $k$ ), were quoted from literature [IEEE Photonic. Tech. L. 2011, 23, 275].<sup>[1]</sup> Because  $k$  of the PET material is very small (on the order of  $10^{-2}$ ), the light is not absorbed after multiple diffraction. This is one of the main reasons for choosing it as the substrate. As described in the main text, here we compare the near-field electric field distribution of structured PET (Fig. S1a) and structured PET with micron-sized scatters on surface (Fig. S1b). It can be found that, regardless of the grating sizes on the PET material, the micro/nano structures on its surface has a great influence on the distribution of the electric field. A universal enhancement can be observed on the structured PET.

In addition, the near-field electric field distribution of different substrates under different wavelengths were also compared, as shown in Figure S2. When we change the wavelength of incident light to 400 nm (Fig. S2a) and 700 nm (Fig. S2b), we can still observe the enhancement of the electric field on the surface of the structured PET with micron-sized scatters.

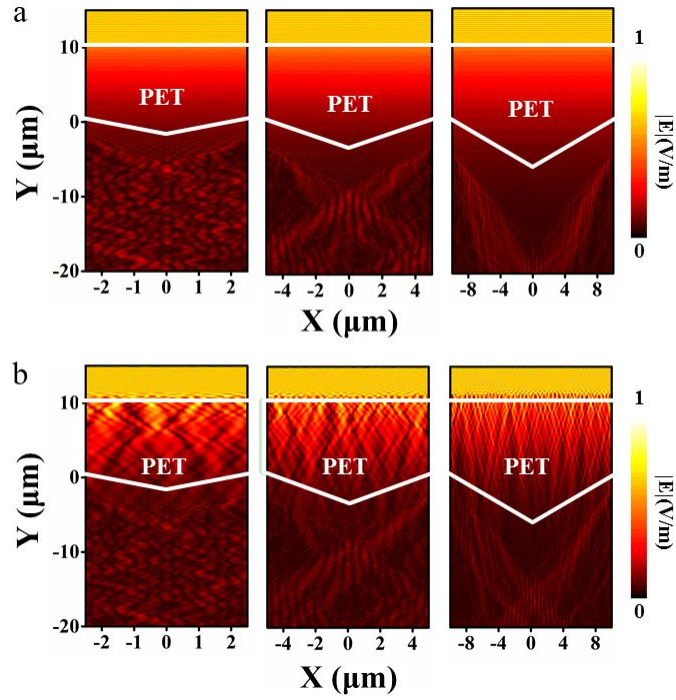


**Figure S1.** The simulated near-field electric field distribution of structured PET (S1a) and structured PET with micron-sized scatters on surface (S1b). The structural parameters are set differently. The incident wavelength was also set as 532 nm.

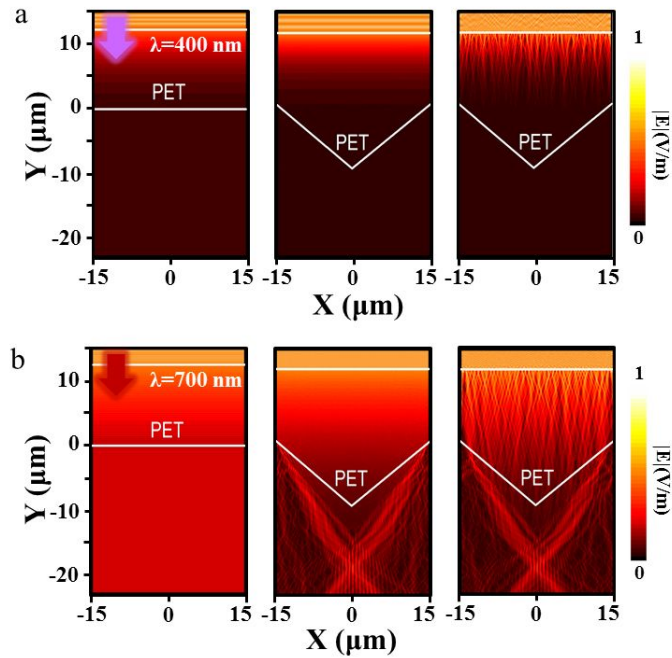


**Figure S2.** The simulated electric field distribution of PET substrates with different structural parameters under the 400 nm light illumination (a) and 700 nm illumination (b).

## Supporting Information S2

### Processing parameters and the corresponding morphologies of grating structures

The SEM images of PET substrates with different structural parameters are shown in Figure S3a. By changing the conditions such as defocusing distance, scanning velocity and laser power, the micro/nano grating structures on PET substrate can be prepared in control. For example, two SEM cross-sectional images of the structured PET substrates with different shapes are shown in Figure S3b. By varying the laser parameters, the grating structures with different widths and depths can be obtained, as listed in Table S1.

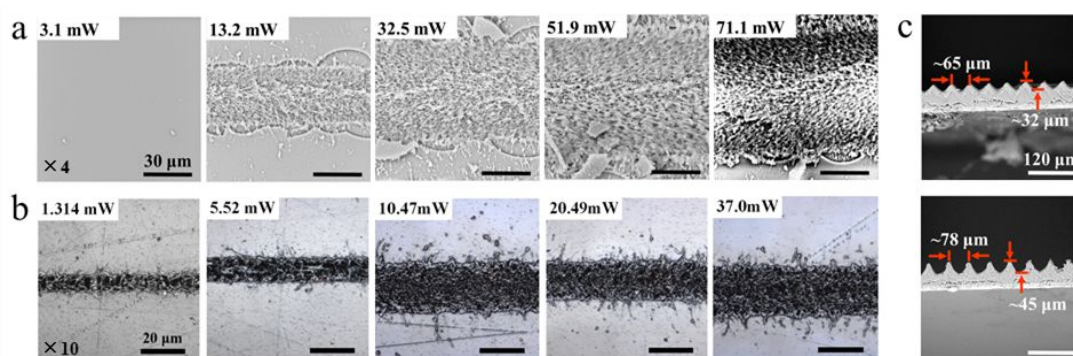


**Figure S3.** (a) The top-view and (b) Cross-section morphologies of grating structures on PET substrates processed by femtosecond laser direct writing. All the images in (a) are the structures that are fabricated under a 4× objective lens. The bottom pictures in (b) are structures fabricated under a 10× objective.

**Table S1.** Processing conditions for different structural parameters.

Magnification, of the objective	Grating Width (μm)	Depth (μm)	Laser Power (mW)	Defocus (μm)	Velocity (mm/s)
×4	25.924	5.944	46.7	0	5
	27.043	18.99	36	100	1
	32.008	11.515	45	50	3
	42.868	12.56	36	350	4
	47.308	15.507	45	250	3

	54.777	18.706	36	400	1
	59.548	8.710	36.6	200	5
	84.898	5.651	45	350	5
	99.564	41.725	45	350	0.5
	101.758	11.602	45	350	2.5

Magnification, of the objective	Grating Width ( $\mu\text{m}$ )	Depth ( $\mu\text{m}$ )	Laser Power (mW)	Defocus ( $\mu\text{m}$ )	Velocity (mm/s)
×10	8.421	0.619	1.314	0	5
	11.975	1.930	5.52	0	5
	15.250	2.856	10.47	0	5
	17.942	3.299	15.75	0	5
	18.473	5.476	20.49	0	5
	20.564	5.117	26.35	0	5
	22.997	5.396	37.0	0	5
	27.022	8.521	52.5	0	5

## Supporting Information S3

### Morphology and XRD characterization of MAPbI<sub>3</sub> perovskite films

The surface morphology of the prepared perovskite films was characterized with SEM images. Figure S4a shows the original data and the processed pictures used in the main text. We use a software (Image-Pro Plus) to determine the thickness and grain size of the film, with ~200 nm and 126 nm, respectively, as shown by the statistical results in Figure S4b. The grain size is similar to that reported in the literature.<sup>[2]</sup>

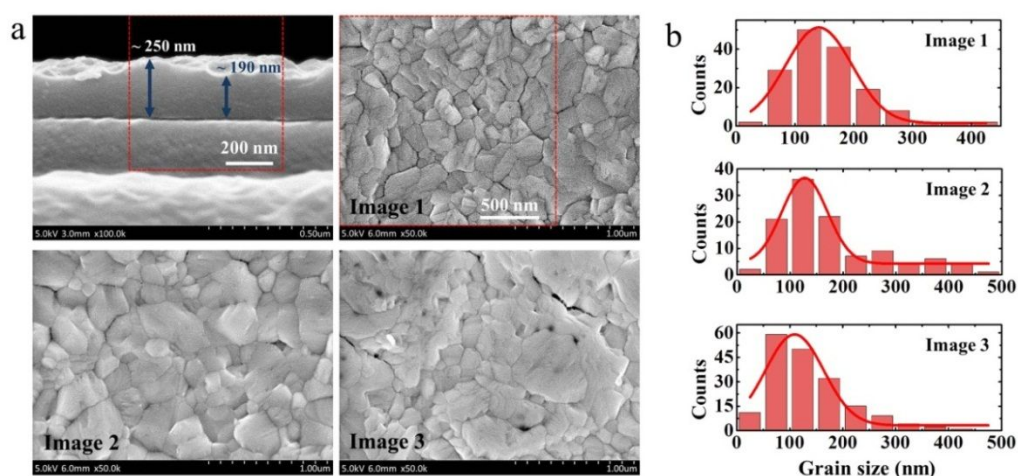


**Figure S4.** (a) Original data and the processed pictures used in the main text. (b) Statistical chart of the grain size of the perovskite films at different positions.

Furthermore, we analyzed the detailed information in the XRD spectrum from 15° to 65°, as shown in Figure S5b. Seven characteristic peaks centered at 19.98°, 28.50°, 31.88°, 40.62°, 43.28°, 50.32°, and 58.90° are assigned to the 112, 220, 310, 224, 330, 404 and 440 planes of the perovskite crystal structure.<sup>[3-4]</sup>

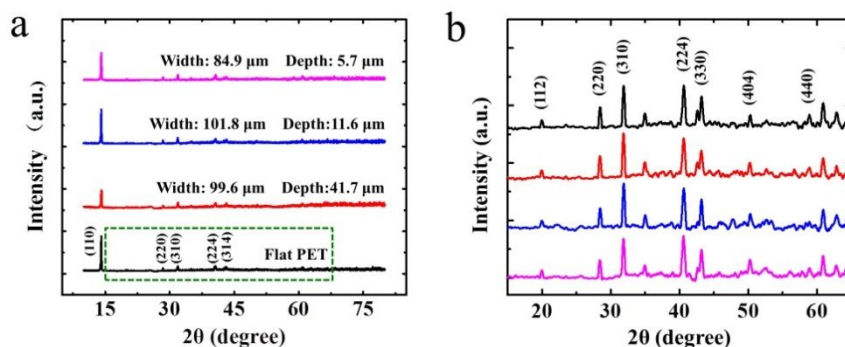


**Figure S5.** (a), (b) XRD pattern comparison of MAPbI<sub>3</sub> film on different substrates.

## Supporting Information S4

### Influence of the structured substrate on the PL life of its surface material

We believe that the processed PET substrate can only change its interaction with the film on its surface but not the properties of the film material itself. In order to verify the above conclusion, photoluminescence (PL) properties of perovskite film on the PET substrates with different widths and depths were compared. Figure S6a presents the 3D confocal microscope images of the processed PET substrates. The PL intensities of perovskite films deposited on the smooth surface of the substrates were studied in detail, as shown in Figure S6b. We found that the structured substrate cannot significantly change the PL intensity of the surface material. The change in the peak position is also negligibly small ( $<5$  nm). However, when we compared the PL lifetime of the perovskite films on different substrates, we found that the lifetime of materials on the structured substrates is indeed slightly longer than that of materials on smooth surfaces, as shown in Figure S6c. In contrast to our previous work, we believe that this similar extension of the PL lifetime is due to the enhanced photon recycling and outcoupling effect caused by the structured substrate.<sup>[5]</sup> However, the change of PL lifetime ( $<5$  ns) is not obvious, which also proves that the substrate has little effect on the properties of the film material itself.

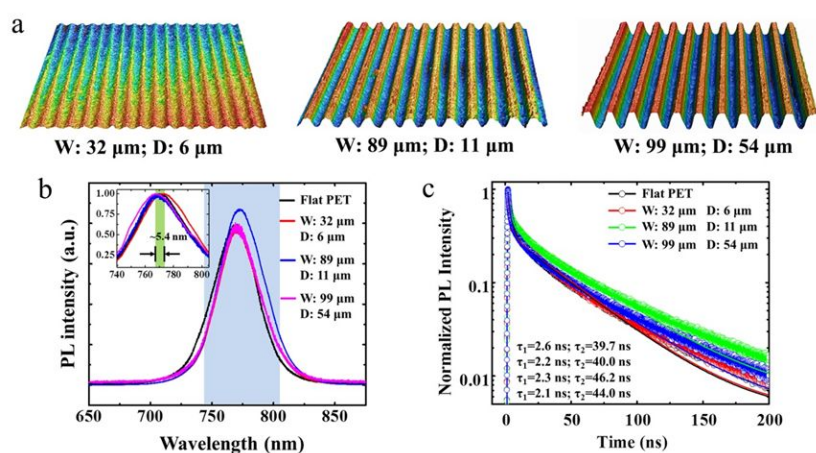


**Figure S6.** (a) 3D confocal microscope images of the processed PET substrates with different structures. (b), (c) PL intensity and lifetime comparison of the perovskite film on different substrates.

## Supporting Information S5

### EQE comparison of perovskite photodetectors with different substrates

In order to explain the physical mechanisms of optoelectronic device performance enhancement, we compared the external quantum efficiency (EQE) of the devices with different substrates. The top-view photographs and schematic diagrams of the devices based on the structured and flat substrate is respectively shown in Figure S7a. Since the area processed by the laser is on the back side of the PET sample, there is no much difference from the images. In our experiments, a xenon lamp with a broad spectrum was used as the light source. The light intensity between 200 and 800 nm is weak but the intensity is relatively stable. When the wavelength is longer than 800 nm, the light intensity is strong but the fluctuation is large, as shown in Figure S7b. This is why the detectivity shown in the main text is fluctuating in this range. With the illumination of this light source, we measured the EQE of different devices, as shown in Figure S7c. The results show that the EQE of the device based on structural substrate (red line) is enhanced within a range of 200-780 nm, which indicates that the periodic micro/nano structures on the substrate have an effective regulation on the carrier transmission of the light-active material on its surface.<sup>[6]</sup> The maximum of enhancement of EQE is about 6.5 times.

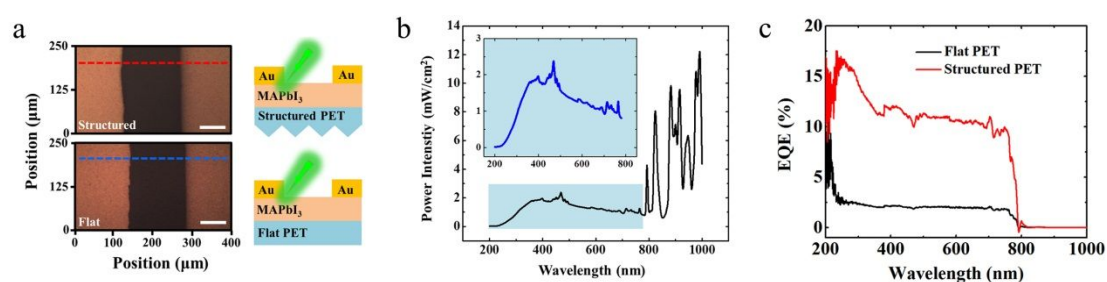


**Figure S7.** (a) Photographs and the schematic diagrams of the devices on the structured (above) and flat (below) PET substrates. The scale bar is 80 μm. (b) Spectral distribution of the light source for wide-range photoresponse. (c) Comparison of EQE of the devices on different substrates.

## Supporting Information S6

### Influence of laser irradiation on the stability of structured FPDs

The thickness of the perovskite film in our FPD was set as  $\sim 200$  nm. The film is so thin that the heat caused by the increasing intensity of incident laser will continuously accumulate at the spot area and in turn cause defects and destructions for the perovskite material. Figure S8a and S8b show the photos and 3D confocal microscope images of the surface morphology of the perovskite film with incident light intensity. It is found that when the laser density is greater than  $1040 \text{ mWcm}^{-2}$ , the ablation caused by the heat accumulation become obvious at the laser spot area. Then, the photoelectric characteristics of FPDs with different ablation degrees on the film surface were measured. The current becomes saturated when the power of the incident laser is larger than  $1500 \text{ mWcm}^{-2}$ , as shown in Figure S8c and S8d. We further compared the currents of the devices before and after strong laser irradiation ( $2500 \text{ mWcm}^{-2}$ ). The FPD will experience an irreversible 30% decrease in photoresponse due to the surface defects and destructions of perovskite materials. In order to further explore the effect of laser on the stability of perovskite materials, we measured the Raman spectra of the samples with different illumination intensities, as shown in Figure S8e. It was observed two typical peaks at  $\sim 69$  and  $104 \text{ cm}^{-1}$ , which are characteristic of the bending mode of I-Pb-I bond and the vibration of MA<sup>+</sup> cation, respectively.<sup>[7-8]</sup> With the increase of incident light power, the peak intensity at  $104 \text{ cm}^{-1}$  increases obviously, which proves that the local structure of the inorganic skeleton of perovskite material has changed during the laser irradiation. The above results show that the laser power can influence the stability of the perovskite devices. Therefore, for our devices, it is suggested to operate under  $1000 \text{ mWcm}^{-2}$ .

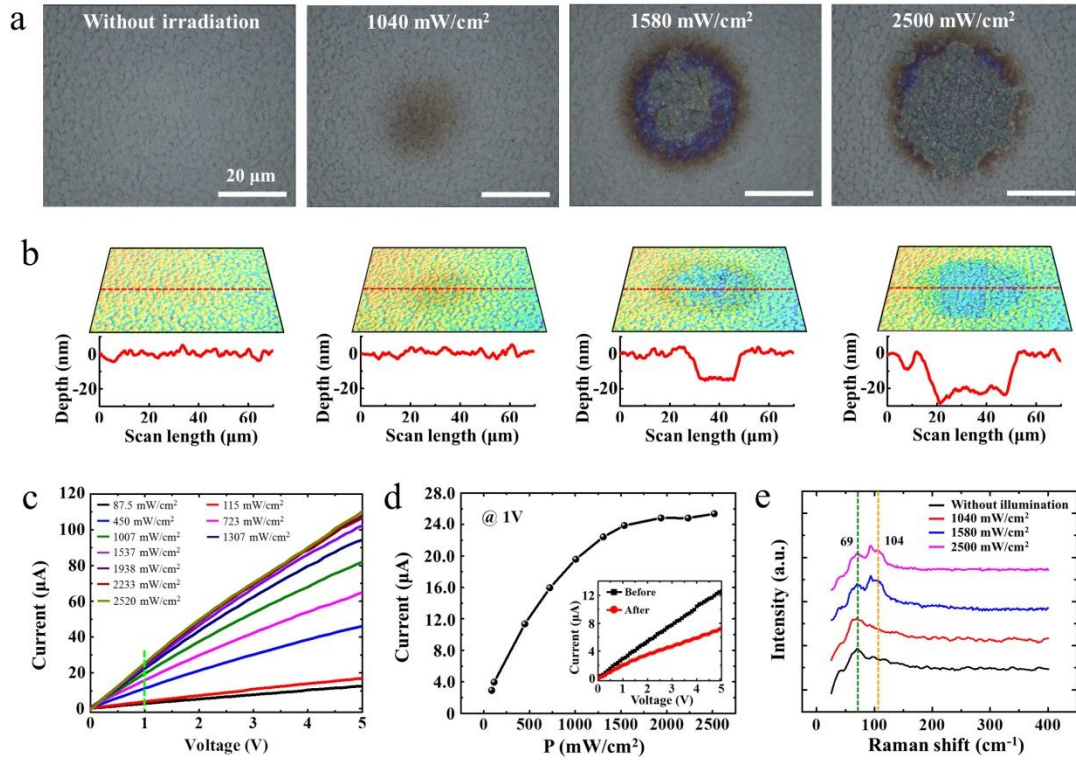


**Figure S8.** (a), (b) Photos and 3D confocal microscope images of the surface morphology of perovskite film with incident light intensity. (c), (d), (e) Photoelectric characteristics and Raman spectra of FPDs under different light intensities.

## Supporting Information S7

### Universal photoresponse enhancement of another back-reflected FPD

Thanks to the near-field optical enhancement of the PET substrates with different grating structures, we found that it can enhance the photoresponse of the perovskite FPDs in general. Here, we also tested the photoelectric characteristic of another device with different structural parameter substrates. Figure S9a shows the 3D morphology of the grating structure on PET substrate. The width is about  $13\ \mu\text{m}$  and the depth is about  $3\ \mu\text{m}$ . Using this structured PET as a substrate, the photoresponse of our photodetector has also been improved by about 2.3 times, as shown in Figure S9b.

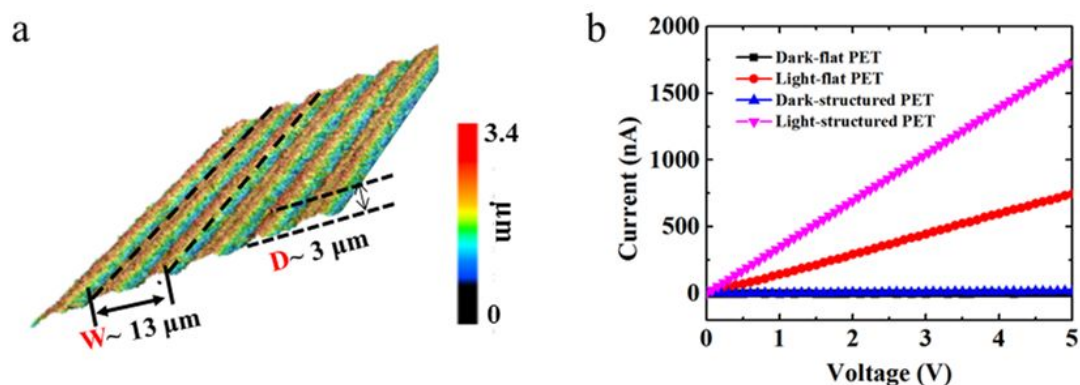


**Figure S9.** (a) The 3D confocal microscope image of the grating structures on PET substrate.

(b) The photoresponse enhancement of another device with different structural parameters.

## Supporting Information S8

### Polarization-dependent photoresponse of the perovskite FPDs

The polarization-dependent photoresponse of our phototetectors were measured. First, the position of the device was fixed and the laser was normally incident on the surface of samples. Then, we gradually rotated the polarization clockwise at a step of 20 degrees from the position parallel to the direction of ripples processed on the PET substrate, as shown in Figure S10a. We carried out two sets of scanning photocurrent imaging (SPI) measurements on the same illumination area (Figure S10b) when the light polarization is parallel and perpendicular to the ripples, respectively. None of the above experiments show that the device has obvious polarization sensitivity. This is mainly because the perovskite film is in-plane isotropic. Although the processed structures on the substrate are unidirectionality, they will not cause the photoelectric anisotropy of the device because the processing size is much larger than the incident light wavelength.

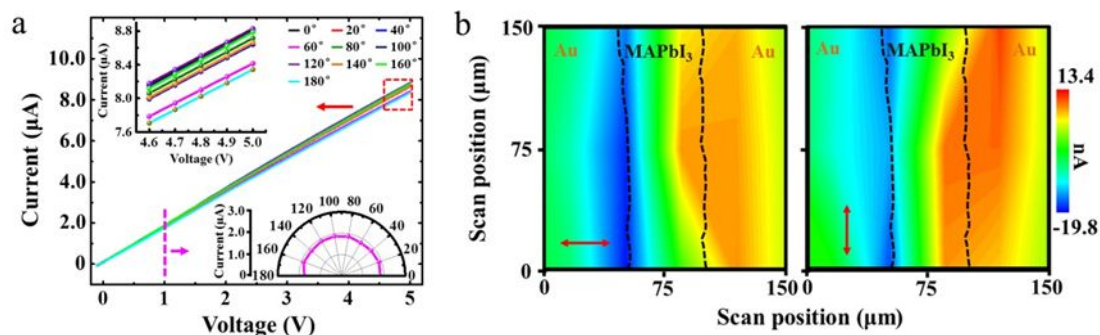


**Figure S10.** (a) Polarization-dependent photocurrent measurements of the perovskite FPDs. (b) SPI experiments of the perovskite FPD under irradiation of the laser with different polarizations (red arrows).

## Supporting Information S9

### FPD Bending performance comparison of devices with different substrates

We measured the bending robustness characteristics of perovskite photodetectors with different substrates. For the devices based on flat PET, there is a significant decrease of the photocurrent when the curvature radius is smaller than 6.48 mm. While for the devices based on structured PET, the photocurrent changes little regardless of the bending conditions, as shown in Figure S11a. To intuitively reveal the influence of the substrate alteration on the bending properties of its surface material, we have observed the surface morphology after bending. Three different viewing areas are marked as red (left), yellow (center) and blue (right), respectively. The photographs and scanning electron microscope (SEM) images are shown in Figure S11b. More cracks on the flat PET based device can be seen. However, the listed micrographs alone are not sufficient to exhibit the degree of damage of the perovskite film caused by the substrate bending. So we made statistics on the change of surface topography in different areas ( $40 \times 40 \mu\text{m}^2$  and  $120 \times 120 \mu\text{m}^2$ ). Four statistical parameters, such as  $S_a$ ,  $S_z$ ,  $S_{pc}$  and  $S_{dr}$  are considered by means of the MultiFile Analyzer software.

Here,  $S_a$ , the arithmetic mean height of surface, is a parameter that characterizes the surface height of the material.  $S_z$ , the maximum surface height, represents the difference between the maximum peak value and the minimum valley value. It can be seen from the Figure S11d that both  $S_a$  and  $S_z$  of perovskite film on structured PET are less than that of flat one, indicating a smaller undulation of the material surface on the structured substrates. In addition,  $S_{pc}$  is arithmetic mean curvature of the peak culmination, and  $S_{dr}$  is developed area ratio of the surface. Both of them represent the surface morphology, and the closer the value to zero, the flatter the surface becomes. From Figure S11d, we can also draw the conclusion that the structured substrate is beneficial to avoid wrinkling of the surface material. With the help of these statistical data, we found that the cracks on the perovskite surface on the structured PET decreased significantly.

The values of  $S_a$ ,  $S_{pc}$  and  $S_{dr}$  can be calculated according to the following formulas:

$$S_a = \frac{1}{A} \iint_A |Z(x, y)| dx dy \quad (1)$$

$$S_{pc} = -\frac{1}{2} \frac{1}{n} \sum_{k=1}^n \left( \frac{\partial^2 z(x, y)}{\partial x^2} + \frac{\partial^2 z(x, y)}{\partial y^2} \right) \quad (2)$$

$$S_{dr} = \frac{1}{A} \left[ \iint_A \left( \sqrt{1 + \left( \frac{\partial z(x, y)}{\partial x} \right)^2 + \left( \frac{\partial z(x, y)}{\partial y} \right)^2} - 1 \right) dx dy \right] \quad (3)$$

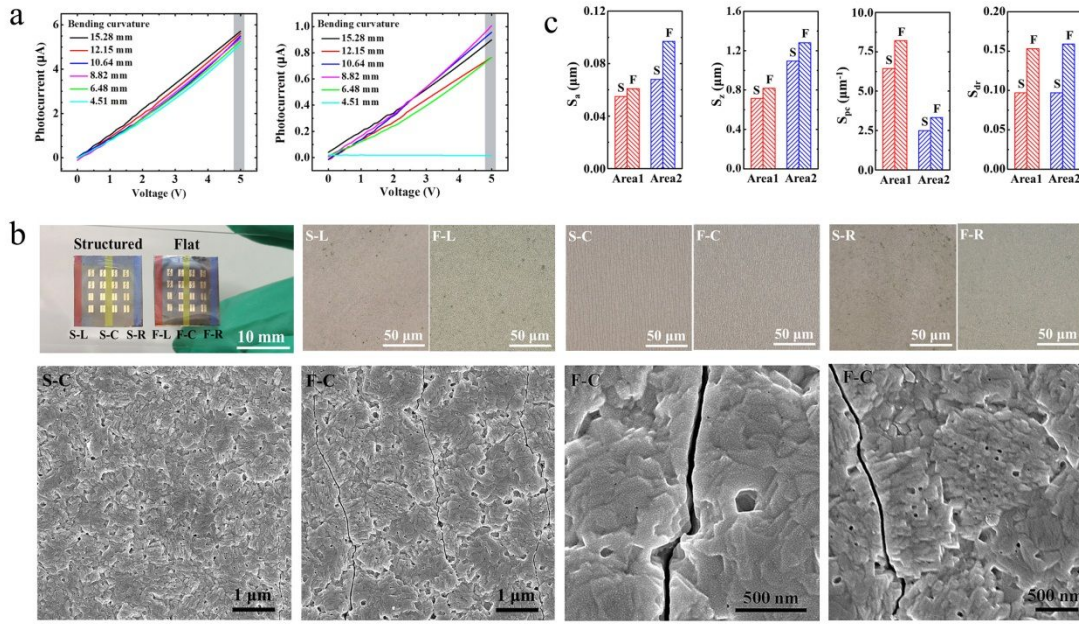


**Figure S11.** (a) I-V characteristics of the devices based on flat and structured PET after bending with different curvature radii. (b) Photographs and SEM images of the devices after 1000 bends in total. The ‘S’ and ‘F’ are abbreviations of ‘structured’ and ‘flat’, respectively. The ‘L’, ‘C’ and ‘R’ are ‘left’, ‘center’ and ‘right’ for short. (c) Data statistics of the cracks on the perovskite surface on different substrates.

In order to further determine the effect of the micro/nanostructures on the substrate on its bending performance, we first simulated the first principal stress distribution in the PET with Comsol Multiphysics software. The width and depth of the sawtooth-shaped grating were determined as 30 μm and 10 μm, respectively. The parameters such as density, Young’s modulus and Poisson’s ratio of PET were set as 1.38 g/cm<sup>3</sup>, 4000 Mpa and 0.338, respectively. A fixed constraint was employed at the left side of the PET layer, and a force of 50 N was loaded at the right side to realize bending of the

PET substrate. Figure S12a shows the whole stress distribution of PET materials with the normalized intensity of pressure ( $\sigma$ ) from -1 to 1. Regardless of the structures on the surface of PET, the stress distribution does not seem to be significantly different. However, when we analyzed the stress distribution according to the different range of intensity, we found that the structures had a great influence on the stress distribution as shown in Figure S12b and S12c. The micro/nanostructures on the structured substrate make the stress distribution more uniform inside the PET material, whereas the stress is more likely to be concentrated on the surface of flat substrate. This is why the perovskite thin film on the flat substrate surface is more likely to be destroyed.

In addition, we also carried out the microstrain ( $\mu\epsilon = (\Delta L/L) \times 10^{-6}$ ) measurements of different PET samples, as shown in Figure S12d. Here,  $\mu\epsilon$  represents one millionth of the strain of the sample,  $L$  for the original length of the cubic element in the sample, and  $\Delta L$  for the change of the length of the cubic element. A platform with four degrees of freedom was used to change the bending curvature of the substrates in steps of 0.25 mm. The data was recorded in real time with an analysis system (DH8302). In our experiment, there are two phenomena worth noting: First, the  $\mu\epsilon$  of the structured PET is much smaller than that of flat one. This means, under the same bending curvature, the stress on the structure PET surface is relatively less. Second, when the bending curvature reached  $\sim 5.5$  mm, the  $\mu\epsilon$  values of both the flat and structured PETs decreased sharply, which indicates the irreversible damage of the material due to excessive stress. This indicates the decline of the device performance below the bending curvature of 5 mm is mainly due to the destruction of the substrates and accompanying cracks of the film material on its surface. However, we can find that micro/nanostructures on the structured substrate can greatly enhance the stability of the device. Figure S12e shows the photoelectric performance of our FPD under further bending. When the bending curvature reaches  $\sim 4.5$  mm, the photocurrent intensity of the device will drop by half. Under this curvature, the photocurrent intensity will further decrease to 20% if the device is bent 100 times. (The discrepancy of the measured stability of the device from that of the main text is due to the different sample used in the supplementary experiment.)

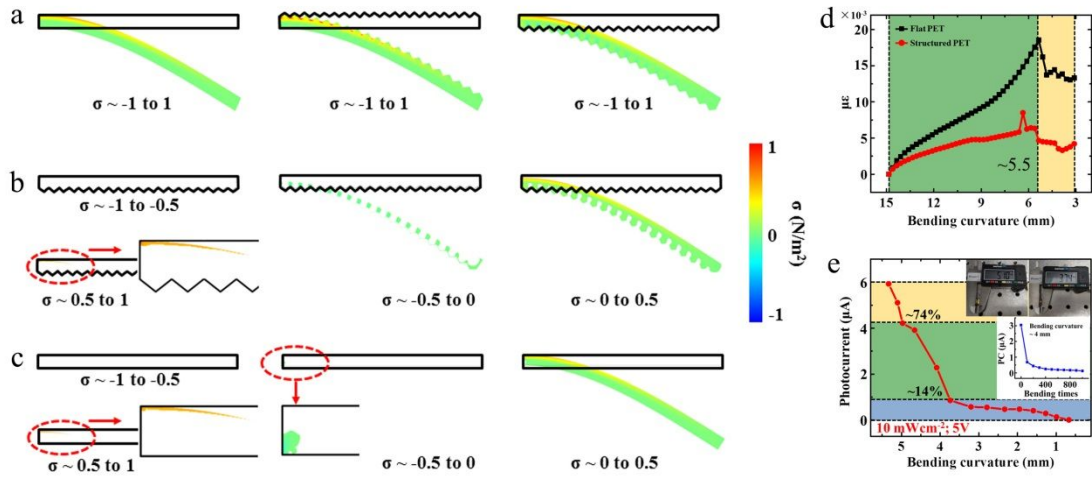


**Figure S12.** (a), (b) and (c) Stress distribution simulation of PET substrates with and without micro/nanostructures under bending. (d) Microstrain measurements of different PET samples. (e) Characterization of bending behaviors of our back-reflected FPD.

## Reference

- [1] Iiyama K.; Ishida T.; Ono Y.; Maruyama T.; Yamagishi T.; Fabrication and Characterization of Amorphous Polyethylene Terephthalate Optical Waveguides. *IEEE Photonic. Tech. L.* **2011**, 23, 275-277.
- [2] Feng J.; Zhu X.; Yang Z.; Zhang X.; Niu J.; Wang Z.; Zuo S.; Priya S.; Liu S. (Frank); Yang D. Record Efficiency Stable Flexible Perovskite Solar Cell Using Effective Additive Assistant Strategy. *Adv. Mater.* **2018**, 30, 1801418.
- [3] Zhao Y.; Zhu K. Charge Transport and Recombination in Perovskite (CH<sub>3</sub>NH<sub>3</sub>)PbI<sub>3</sub> Sensitized TiO<sub>2</sub> Solar Cells. *J. Phys. Chem. Lett.* **2013**, 4, 2880-2884.
- [4] Zhang Y.; Du J.; Wu X.; Zhang G.; Chu Y.; Liu D.; Zhao Y.; Liang Z.; Huang J. Ultrasensitive Photodetectors Based on Island-Structured CH<sub>3</sub>NH<sub>3</sub>PbI<sub>3</sub> Thin Films. *ACS Appl. Mater. Interfaces*, **2015**, 7, 21634-21638.
- [5] Xing J.; X Zheng.; Yu Z.; Lei Y.; Hou L.; Zou Y.; Zhao C.; Wang B.; Yu H.; Pan D.; Zhai Y.; Cheng J.; Zhou D.; Qu S.; Yang J.; Ganeev R. A.; Yu W.; Guo C. Dramatically Enhanced Photoluminescence from Femtosecond Laser Induced Micro-/Nanostructures on MAPbBr<sub>3</sub> Single Crystal Surface. *Adv. Opt. Mater.* **2018**, 6, 1800411.
- [6] Kelzenberg M. D.; Boettcher S. W.; Petykiewicz J. A.; Turner-Evans D. B.; Putnam M. C.; Warren E. L.; Spurgeon J. M.; Briggs R. M.; Lewis N. S.; Atwater H. A. Enhanced Absorption and Carrier Collection in Si Wire Arrays for Photovoltaic Applications. *Nat. Mater.* **2010**, 9, 239-244.

- [7] Gottesman R.; Gouda L.; Kalanoor B. S.; Haltzi E.; Tirosh S.; Rosh-Hodesh E.; Tischler Y.; Zaban A. Photoinduced Reversible Structural Transformations in Free-Standing  $\text{CH}_3\text{NH}_3\text{PbI}_3$  Perovskite Films. *J. Phys. Chem. Lett.* **2015**, *6*, 2332-2338.
- [8] Quarti C.; Grancini G.; Mosconi E.; Bruno P.; Ball J. M.; Lee M. M.; Snaith H. J.; Petrozza A.; Angelis F. De. The Raman Spectrum of the  $\text{CH}_3\text{NH}_3\text{PbI}_3$  Hybrid Perovskite: Interplay of Theory and Experiment. *J. Phys. Chem. Lett.* **2014**, *5*, 279-284.